

# 1 Generation of CW mid-infrared radiation in the 2 mW power range and tuneable over 400 nm

3 RICCARDO BRAMERI,<sup>1,\*</sup> VALERIO VITALI,<sup>1</sup> LUDOVIC  
4 GAUTHIER-MANUELAND,<sup>2</sup> COSIMO LACAVALA,<sup>1</sup> FEDERICO PIRZIO,<sup>1</sup>  
5 ANTONIANGELO AGNESI,<sup>1</sup> MATHIEU CHAUVET<sup>2</sup> AND ILARIA  
6 CRISTIANI<sup>1</sup>

7 <sup>1</sup>*Department of Electrical, Computer and Biomedical Engineering, University of Pavia, Pavia, 27100, Italy*

8 <sup>2</sup>*FEMTO-ST institute, UMR CNRS 6174, University of Franche-Comté, 15B Avenue des Montboucons,  
9 25030 Besançon, France*

10 *\*riccardo.brameri01@universitadipavia.it*

11 **Abstract:** Miniaturization of mid-infrared (MIR) spectroscopy sources has progressed  
12 significantly during the past two decades, but a solution able to provide full integration, high  
13 optical power and wide tuneability in the so-called atmospheric window (2.5 - 5  $\mu\text{m}$ ) is still  
14 missing. In this context, we investigated a broadband frequency-tuneable source relying on  
15 difference frequency generation (DFG) in a periodically poled Lithium Niobate (PPLN) ridge  
16 waveguide. By employing tuneable lasers for the pump and signal wavelengths emitting at  
17 around 1  $\mu\text{m}$  and 1.55  $\mu\text{m}$ , respectively, we were able to fully cover the  $\approx 3 - 3.5 \mu\text{m}$  spectrum,  
18 thus translating the technological maturity of data communication photonic sources to the MIR  
19 wavelength band. Moreover, the use of a relatively large cross-section for the here-proposed  
20 PPLN ridge waveguide compared to commonly employed thin-film Lithium Niobate (TFLN)  
21 waveguides has allowed us to achieve low propagation and coupling losses together with high  
22 damage threshold, thereby allowing us to reach mW-level power in the MIR wavelength band.

## 23 1. Introduction

24 Mid-infrared (MIR) optical sensors based on spectroscopy represent powerful tools in several  
25 applications, such as environmental monitoring, industrial process control and petrochemical  
26 industry [1, 2]. The ability to accurately identify different chemical species requires the use  
27 of laser sources with spectral lines in the kHz range, output powers of several mW, and fine  
28 tuneability in frequency over an extended band of the order of several tens of nm. In particular,  
29 the so-called atmospheric window that ranges from 2.5 to 5  $\mu\text{m}$  is of high interest as it contains  
30 the spectral fingerprints of several pollutants, such as  $\text{N}_2\text{O}$ ,  $\text{CO}_2$ ,  $\text{NO}_2$ ,  $\text{HCl}$ ,  $\text{NH}_3$ ,  $\text{C}_2\text{H}_6$  and  
31 others. The availability of a widely tuneable and powerful MIR source suitable for integration  
32 on a photonic integrated circuit (PIC) platform and for mass production is still missing and  
33 would represent a revolutionary opportunity in this rapidly expanding application area. Important  
34 technological advances for MIR spectroscopy have been the development of room-temperature  
35 quantum cascade lasers (QCL) [3–5] and interband cascade lasers (ICL) [6, 7], which have  
36 extended the operating range of tuneable semiconductor lasers from the visible and near-infrared  
37 (NIR) to the MIR. With these sources, a novel generation of sensors suitable for real-time in  
38 situ detection of gases is now available. However, such tools, which rely on the assembly of  
39 discrete optical components, still fail to meet some key requirements for many applications. The  
40 first limitation is related to their limited tuneability, which usually limits their application to the  
41 detection of a single species for a given laser source.

42 In the present scenario, the exploitation of efficient nonlinear integrated photonic platforms could  
43 represent an appealing solution for MIR light generation and amplification with a very compact  
44 footprint [8, 9]. Indeed, the exploitation of nonlinear processes could allow to efficiently translate  
45 the radiation emitted by mature and low-cost telecom optical sources, with excellent linewidth

46 properties, modulation capabilities and wide tuneability, to the MIR spectral region.

47 Lithium Niobate (LN) is one of the most mature material platforms for the realization of  
48 second-order nonlinearity-based integrated photonic devices [10, 11]. In recent years, a few  
49 results have been reported on the generation of continuous wave (CW) and tuneable MIR  
50 radiation exploiting LN-on-insulator (LNoI) platforms. Nonlinear waveguides usually rely on  
51 ridge structures obtained by dry etching a very thin LN core layer (typically 300 - 900 nm  
52 thick [12–14]) bonded on top of a silica cladding. Such geometry allows obtaining strong modal  
53 confinement devices, which were not available in the past; this fuelled a significant research  
54 activity based on the exploitation of the LNoI platform for nonlinear applications. The strong  
55 modal confinement and flexibility in the waveguide geometry and cladding materials offered  
56 by the LNoI platform guarantees new degrees of freedom in tailoring waveguide dispersion,  
57 enabling both frequency generation over an ultra-wide bandwidth [15] and intermodal phase  
58 matching for multi-wavelength generation in a single waveguide [16]. Despite its outstanding  
59 efficiency and versatility, the LNoI platform suffers from some fundamental limitations. Indeed,  
60 the typically strong modal mismatch between focused input beams and LNoI waveguide modes  
61 at the integrated chip facet commonly results in a very poor butt-coupling efficiency of pump  
62 and signal. Typical reported values are in the order of  $\sim 1 - 2\%$  [17], which makes this factor  
63 relevant when considering the nonlinear performance of the system [18]. In principle, better  
64 coupling efficiency can be obtained by the exploitation of grating or edge couplers with advanced  
65 designs at the expense of an increased complexity in the waveguide fabrication and a limitation  
66 in the operational bandwidth. Moreover, huge field intensities result from the extreme mode  
67 confinement in the LNoI waveguides (mode effective area = 0.2 - 1.5  $\mu\text{m}^2$ ), which allows  
68 achieving very high nonlinear efficiencies. However, absolute values of the MIR output power in  
69 the order of a few tens of  $\mu\text{W}$  are typically reported, which are insufficient for most spectroscopy  
70 applications. In this work, we demonstrate the generation of MIR radiation through difference  
71 frequency generation (DFG) tuneable from 3 to 3.5  $\mu\text{m}$  with output power in the mW range. This  
72 result is obtained by exploiting a nonlinear LNoI platform based on a ridge waveguide with a  
73 cross-section enabling optimal coupling efficiency and low propagation losses for the wavelengths  
74 involved in the nonlinear process. This ridge structure consists of a periodically poled LN crystal  
75 that guarantees phase-matched interactions over a band exceeding 400 nm. We believe that the  
76 proposed device can represent a significant breakthrough towards the development of integrated  
77 CW sources able to provide high-power and tuneable radiation in the MIR range for spectroscopy  
78 applications.

## 79 2. Design and simulations

80 The proposed device is based on the use of the DFG process exploiting the high second-order  
81 nonlinear coefficient  $d_{33}$  (25.2 pm/V) of LN. Considering a pump wave at a wavelength  $\lambda_p$   
82 and a signal at a wavelength  $\lambda_s$ , the wavelength  $\lambda_i$  of the generated radiation (idler) is obtained  
83 according to the energy conservation principle:

$$\frac{1}{\lambda_i} = \frac{1}{\lambda_p} - \frac{1}{\lambda_s} \quad (1)$$

84 By considering a pump wavelength  $\lambda_p$  ranging from 1 to 1.1  $\mu\text{m}$  and a signal tuneable in the  
85 optical communication C-band (1.53 - 1.565  $\mu\text{m}$ ), a MIR radiation in the range from 2.75 to  
86 3.91  $\mu\text{m}$  could be generated. The efficiency of the nonlinear process is mainly dictated by the  
87 phase matching (PM) condition that has to be fulfilled between the interacting fields. As already  
88 extensively reported in the literature, such a condition can be satisfied by periodically poling the  
89 ferroelectric domains of the LN waveguide. In this case, the phase-matching condition can be  
90 written as [19]:

$$\Delta\beta = \beta_p - \beta_s - \beta_i - \frac{2\pi}{\Lambda} \approx 0, \text{ with } \beta_j = \frac{2\pi n_{eff,j}}{\lambda_j}, \quad (2)$$

91 where  $\Delta\beta$  is the phase-mismatch term,  $\beta_j$  is the propagation constant of the fundamental  $TM_{00}$   
 92 mode employed in this work at the pump (p), signal (s) and idler (i) wavelengths,  $n_{eff,j}$  is the  
 93 effective refractive index,  $\lambda$  is the wavelength and  $\Lambda$  is the poling period selected to achieve the  
 94 phase-matching. The designed ridge waveguides exhibited a cross-section of  $7 \times 9.6 \mu\text{m}^2$  and  
 95 was 3 cm-long. Since the inversion of the ferroelectric domains is induced by placing a mask on  
 96 top of the LN wafer, the orientation of the poling requires to couple the radiation as transverse  
 97 magnetic (TM). The waveguides are placed on a  $0.6 \mu\text{m}$  silicon dioxide ( $\text{SiO}_2$ ) layer, bonded  
 98 through a  $0.2 \mu\text{m}$  gold (Au) layer to a silicon (Si) wafer (see Fig. 1a). The spatial distribution of  
 99 the fundamental  $TM_{00}$  mode in the wavelength ranges of  $\lambda_p = 1 - 1.1 \mu\text{m}$ ,  $\lambda_s = 1.53 - 1.57 \mu\text{m}$   
 100 and  $\lambda_i = 2.7 - 4 \mu\text{m}$ , their respective effective refractive indices and effective areas were obtained  
 101 through numerical simulations based on a commercial software (MODE Solutions from ANSYS  
 102 Inc.). The mode field diameters (MFDs) simulated at  $\lambda_p = 1 \mu\text{m}$  and  $\lambda_s = 1.55 \mu\text{m}$  were  $6.248$   
 103  $\mu\text{m}$  and  $6.303 \mu\text{m}$ , respectively, thus providing a very good mode matching with the fundamental  
 104 mode of the optical fiber used for edge coupling (MFD =  $6.6 \mu\text{m}$  @  $1 \mu\text{m}$ ). From the numerical  
 105 simulations performed at  $\lambda_i = 4 \mu\text{m}$ , it can be seen that the fundamental  $TM_{00}$  mode (see Fig.  
 106 1b) is very well confined in the LN ridge waveguide with a MFD of  $6.631 \mu\text{m}$  and with a limited  
 107 extent into the silica layer, thus limiting additional losses that might arise at MIR wavelengths  
 108 due to the  $\text{SiO}_2$  cladding material absorption. Additionally, it is worth noting that the mode size  
 109 is weakly dependent on wavelength, resulting in an optimal spatial overlap between the three  
 110 interacting wavelengths.

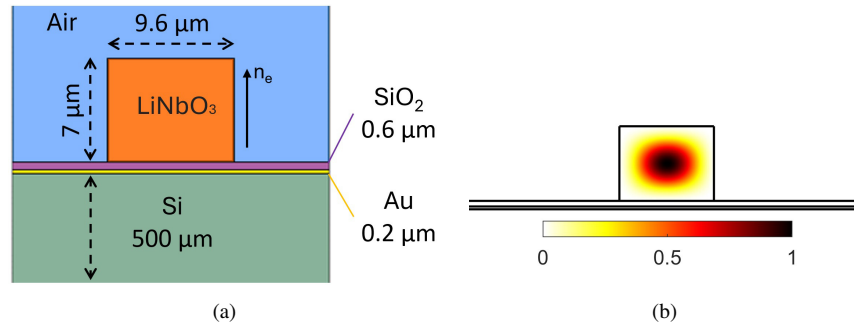


Fig. 1. (a) Cross-sectional view of the designed waveguide and dimensions; (b) Spatial distribution of the electric field of the fundamental  $TM_{00}$  mode numerically simulated at  $4 \mu\text{m}$ .

111 The poling period was determined through numerical simulations to achieve quasi-phase  
 112 matching across the desired wavelength range, with the results reported in Fig. 2a. Fig 2b reports  
 113 the phase-mismatch diagram that can be obtained considering a poling period equal to  $25 \mu\text{m}$ . In  
 114 this configuration, the phase-matching for the DFG nonlinear process can be preserved over a  
 115 broad wavelength range from  $2.7$  to  $3.5 \mu\text{m}$  by tuning the pump wavelength. By considering a  
 116 LN waveguide with a different poling period, it is possible to shift the phase matching band to  
 117 longer or shorter wavelengths.

118 The coupling efficiencies between a cleaved fiber (MFD =  $6.6 \mu\text{m}$  @  $1 \mu\text{m}$ , as in the experiments)  
 119 and the fundamental and higher-order TM modes of the designed LN waveguide were numerically  
 120 calculated. The overall coupling efficiency was found to be equal to  $80\%$ , with most of the power  
 121 coupled to only two modes:  $73.2\%$  of the total power was coupled into the  $TM_{00}$  mode and  $6.2\%$   
 122 was coupled into the  $TM_{02}$  mode. The maximum coupling to all the other modes was found to be  
 123 negligible.

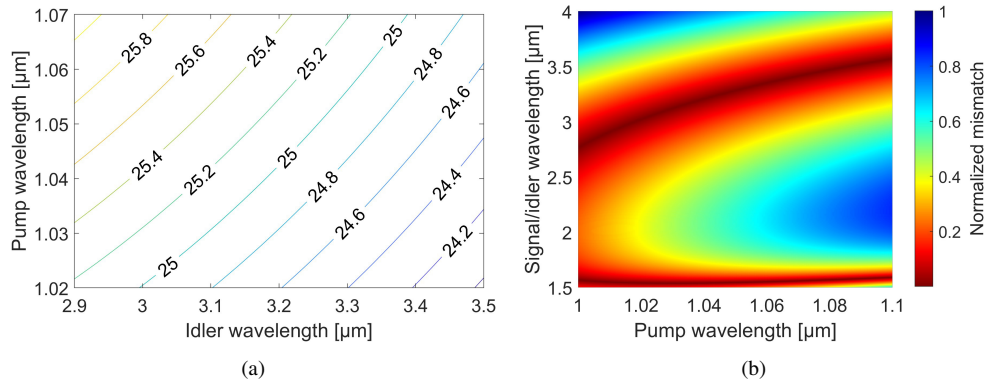


Fig. 2. (a) Numerical simulations of the required poling period (in  $\mu\text{m}$ ) to satisfy the phase-matching condition as a function of the pump and idler wavelengths considering a signal wavelengths in the range 1530 - 70 nm; (b) Normalized phase mismatch diagram numerically simulated for a poling period equal to 25  $\mu\text{m}$ .

### 124 3. Fabrication

125 The first stage of the fabrication was to periodically pole a 500  $\mu\text{m}$  thick, 4 inches diameter  
 126 commercial z-cut congruent  $\text{LiNbO}_3$  wafer by a standard technique involving the application of  
 127 an intense electric field at room temperature [20] using a photo-resist pattern [Fig. 3 (a)]. Several  
 128 poling periods near 25  $\mu\text{m}$  were inserted in the mask and realized to keep into account fabrication  
 129 variations. In a subsequent stage, a  $\text{SiO}_2$  layer was deposited by ICPECVD (Inductively-Coupled  
 130 Plasma-Enhanced Chemical Vapour Deposition) onto one face of the poled wafer followed by  
 131 the sputtering of a 100 nm-thick gold layer [Fig. 3 (b)]. A high-flatness silicon wafer was also  
 132 coated with a 100 nm-thick gold layer. The metallized faces of both the PPLN and silicon wafers  
 133 were then placed into contact and pressed in a wafer bonding machine [Fig. 3 (c)]. This metal  
 134 diffusion bonding process was realized at room temperature which prevents mechanical stress  
 135 that could occur due to the dissimilar temperature coefficients of the two wafers. The bonding  
 136 procedure was completed by applying a strong pressure to the stack which yields more than  
 137 98% of the surface bonded, as observed by an ultrasound characterization technique. At the  
 138 end of the process, a 1 mm thick hybrid structure composed of a silicon substrate bonded to a  
 139 PPLN wafer is obtained. The structure was mechanically polished to obtain a 7  $\mu\text{m}$  thick PPLN  
 140 layer [Fig. 3 (d)]. Note that this method was used earlier to produce adhered non-linear ridge  
 141 waveguides [21–23] where either epoxy glue or direct bonding was used to fix the PPLN wafers  
 142 onto  $\text{LiNbO}_3$  or  $\text{LiTaO}_3$  substrates. At this stage, the layers' thickness was examined to select the  
 143 most homogeneous areas on the wafer. In the next step, two parallel trenches were cut in the  
 144 PPLN layer by a precision dicing saw to form the lateral sides of the ridge waveguide [Fig. 3 (e)].  
 145 The dicing parameters were set to minimize the roughness of the cut surfaces [24, 25]. Finally,  
 146 the hybrid wafer was diced to achieve polished input and output faces for the ridge waveguides.

### 147 4. Experimental setup

148 A schematic of the experimental setup used for the device characterization is reported in Fig. 4. It  
 149 consists of a fiberized input side to couple the optical pump and signal into the PPLN waveguide  
 150 and a free-space detection side to collect the output beams.

151 A custom-made CW tuneable laser source, able to generate Watt-level optical power in the  
 152 wavelength band 1020 - 1065 nm, was employed as the optical pump. The laser consists of an  
 153 oscillator with 6 mW maximum output power amplified through a co-propagating amplification

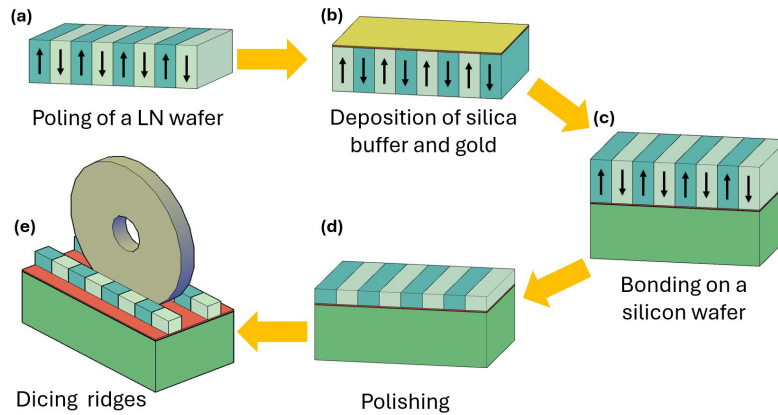


Fig. 3. Fabrication schematic: (a) periodically poling of a LiNbO<sub>3</sub> wafer; (b) deposition of silica and sputtering of gold buffer; (c) bonding of the PPLN wafer on a silicon wafer; (d) grinding and polishing of the PPLN side to reach the desired thickness; (e) dicing of the ridge waveguides and of the hybrid wafer.

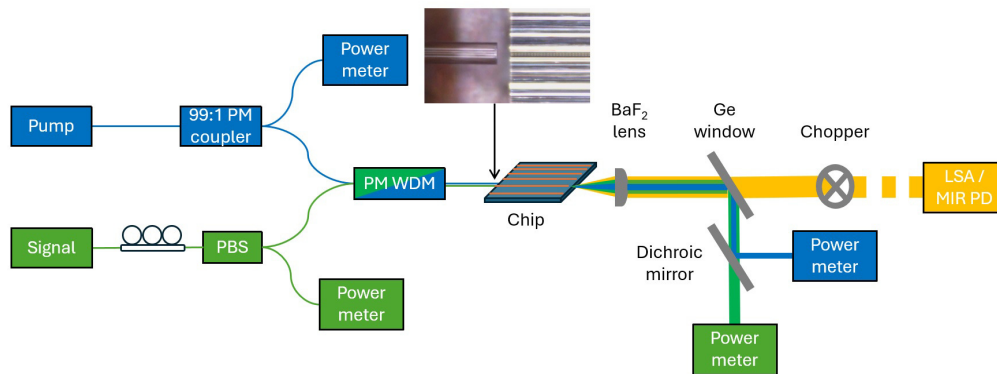


Fig. 4. Experimental setup used for the nonlinear DFG experiments. The photo shows the edge-coupling between a cleaved optical fiber and a PPLN waveguide. PBS: polarization beam splitter, PM WDM: polarization-maintaining wavelength division multiplexer, PM coupler: polarization-maintaining coupler, LSA: laser spectrum analyser, MIR PD: MIR photodiode. The fiberized/free-space blue, green and orange lines indicate the paths of the pump, signal and idler beams, respectively.

154 stage. The oscillator's active medium is a Yb-doped polarization-maintaining (PM) optical  
 155 fiber pumped with a 300 mW laser diode at 976 nm. The emission wavelength is set with a  
 156 1200-lines/mm grating mirror. The output of the oscillator, from a fiber coupler, is sent through  
 157 a pump combiner to a double-clad Yb-doped PM amplifier pumped by a 10-W single-emitter  
 158 multimode laser diode at 915 nm. The amplified output is separated from the residual pump by  
 159 a dichroic mirror and an isolator is added to avoid back reflections into the oscillator. A  $\lambda/2$   
 160 waveplate and a C-coated lens are used to couple the laser output radiation in a PM optical fiber,  
 161 which is then connected to a 99:1 PM fiber coupler. The power of the pump laser is monitored  
 162 through a power meter that detects the 1% output of the 99/1 PM fiber coupler. The signal beam  
 163 is generated by a CW laser (hp8168F) tuneable in the S-C bands, with a 100 kHz linewidth and  
 164 0.035 nm tuning accuracy. The signal is then amplified using an Erbium-doped fiber amplifier

165 (EDFA) with maximum output power of 1W. Since the laser and the EDFA are not PM devices,  
166 a manual fiber polarization controller and a fiber polarization beam splitter (PBS) are used to  
167 precisely control the polarization of the signal coupled into the PPLN waveguide. The PBS  
168 limits the maximum signal power to around 500 mW. The polarization extinction is controlled by  
169 monitoring the power on one output of the PBS using a power meter. The pump and signal are  
170 combined together with a PM wavelength division multiplexer (WDM). The light is coupled into  
171 the PPLN waveguides through edge-coupling using a cleaved PM fiber (fiber PM980-XP), whose  
172 angle is controlled using a fiber rotator to excite the fundamental  $TM_{00}$  mode of the waveguide.  
173 The chip is mounted on a metal support equipped with a Peltier cell which can be used to change  
174 the temperature.

175 In the edge-coupling procedure, the spatial modes at the optical pump wavelength at the chip  
176 output facet were imaged using a CCD camera (Thorlabs DC1545M-G1) to maximize the power  
177 coupled into the  $TM_{00}$  mode of the waveguide. A free-space coupling scheme is set up to collect  
178 the output radiation from the chip using a  $BaF_2$  lens with an anti-reflective coating between 2 - 5  
179  $\mu\text{m}$  to initially collimate the output light. The different wavelength components of the collimated  
180 output beam are split using a germanium (Ge) window with an anti-reflective coating between  
181 1.9 - 6  $\mu\text{m}$  and a dichroic mirror. The pump and signal beams are measured using two power  
182 meters (Ophir 3A-SH and Thorlabs PM16-122, respectively). The MIR beam component is  
183 modulated using a chopper and it is then measured initially through a laser spectrum analyser  
184 (BRISTOL 771-B MIR) to determine the wavelength of the generated idler and then using an  
185 InAsSb photodiode (Thorlabs PDA07P2) to retrieve the MIR power at the corresponding idler  
186 wavelengths. The modulated signal from the InAsSb photodiode is finally acquired through a  
187 USB oscilloscope (Digilent Analog Discovery 2).

## 188 5. Waveguide characterization

189 A linear characterization of the waveguides was initially carried out by measuring the waveguide  
190 propagation losses using the Fabry-Perot interferometric method, utilizing both fringe contrast  
191 and Fourier analysis [26]. We measured propagation losses in the S- and C-bands of  $\approx 0.026$   
192 dB/cm. The coupling losses were also evaluated and we measured coupling efficiency of  $\approx 75\%$   
193 using a simple  $90^\circ$ -cleaved optical fiber, in good agreement with numerical simulations. These  
194 results highlight the advantages of using large waveguides compared to commonly used thin-film  
195 LN (TFLN) waveguides, both in terms of propagation and coupling losses. In particular, the high  
196 coupling efficiency was achieved without the use of lensed optical fibers thanks to the similar  
197 MFD of the PPLN waveguide and the single-mode fiber, thus providing even better long-term  
198 power stability in the experiments thanks to the relaxed tolerance in terms of fiber misalignment.  
199 Nonlinear experiments were then carried out on a 3 cm-long PPLN waveguide with a poling  
200 period of 24.6  $\mu\text{m}$ , and side dimensions of  $7 \times 9.6 \mu\text{m}^2$ .

201 The overall conversion bandwidth was evaluated by varying the pump wavelength  $\lambda_p$  at 5  
202 nm steps from 1020 to 1065 nm. The signal wavelength  $\lambda_s$  was fine-tuned across the EDFA  
203 amplification spectrum for each  $\lambda_p$  value. The results of this characterization are reported  
204 in Fig. 5a (note that values indicated in the figure are normalized and refer to absolute MIR  
205 power values between 220 and 300  $\mu\text{W}$  that are dependent on the pump power availability at  
206 the specific wavelength of operation). As expected from numerical simulations, we observed  
207 that the maximum efficiency of the DFG process remains almost constant over a wide band in  
208 the MIR, approximately 460 nm. By finely tuning the wavelengths of both the pump and signal,  
209 it is possible to achieve the maximum efficiency for any desired MIR wavelength within this  
210 bandwidth. According to numerical simulations, using laser sources for the pump and signal  
211 with a broader tuneability, the range of the generated idler wavelengths could be further enlarged.  
212 The recorded peak normalized efficiency is equal to 3.24  $\%/W/\text{cm}^2$ , while the simulated one is  
213 equal to 6.73  $\%/W/\text{cm}^2$ . The efficiency is normalized by accounting for C-band losses and the

214 nonlinear effective length of the waveguide, as in Ref. [15]. The nonlinear effective length of the  
 215 waveguide accounts for the length of the waveguide over which the phase-matching condition can  
 216 be considered actually satisfied and an effective nonlinear process takes place. This was evaluated  
 217 by fixing the wavelength of the pump and varying the wavelength of the signal to retrieve the  
 218 signal-conversion bandwidth. By comparing the measured full width at half maximum (FWHM)  
 219 to the simulated one, an effective length of  $\approx 70\%$  of the total waveguide length was found. The  
 220 reason behind this could be variations in the size and poling period along the waveguide. The  
 221 difference between simulated and experimentally measured efficiencies could be likely attributed  
 222 to higher MIR losses compared to the C-band losses and also to the limited nonlinear effective  
 223 length of the waveguide. Through a comparison between experimental and simulated efficiencies,  
 224 it is also possible to determine the maximum value of the loss in the MIR being equal to 1.5  
 225 dB/cm, by setting a nonlinear effective length equal to 70% of the real waveguide length.

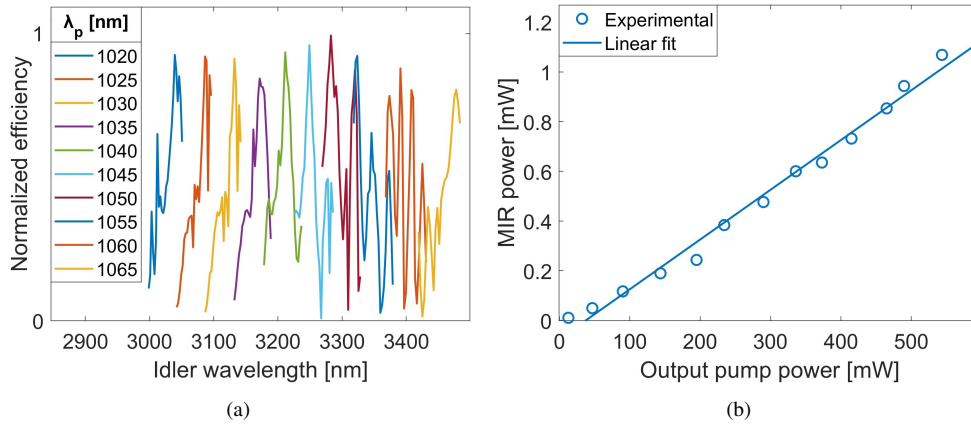


Fig. 5. (a) Normalized conversion efficiency as a function of the idler wavelength for different wavelengths of the pump source; (b) Idler output power as a function of the output pump power. The input signal power is fixed at 0.5 W; the wavelengths are set as:  $\lambda_p = 1040$  nm,  $\lambda_s = 1537.8$  nm and  $\lambda_i = 3212.76$  nm.

226 To evaluate the idler output power as a function of the pump power, we set the pump wavelength  
 227  $\lambda_p = 1040$  nm, the signal wavelength  $\lambda_s = 1537.8$  nm with an EDFA output power  $P_s = 0.5$  W  
 228 and we continuously varied the pump power, recording the idler output power at  $\lambda_i = 3212.76$   
 229 nm. The results are reported in figure 5b. The output idler power grows linearly with the pump  
 230 power up to the mW level, which satisfies the typical power requirements for direct absorption  
 231 spectroscopy (DAS). DAS is one of the simplest methods for trace gas analysis and consists of  
 232 the detection of a residual MIR beam that has propagated through a gas sample. The typically  
 233 minimum required power for nearly shot-noise-limited MIR detection is of the order of 0.1 mW,  
 234 depending on the detector [27]. Due to the input pump power limit in this test, we did not reach  
 235 the saturation point of the conversion that we analytically estimated would be reached with a  
 236 pump power in excess of 20 W, nor the damage threshold of the waveguide. By considering a  
 237 similar waveguide structure [28], we estimate that the maximum power we could tolerate inside  
 238 the waveguide before reaching the damage threshold is 4 W (CW regime), occurring considerably  
 239 sooner than the pump depletion-induced saturation point. Therefore, we can assume that is  
 240 possible to generate even higher MIR optical power with the proposed device.

## 241 6. Conclusion

242 In conclusion, we discussed the design, fabrication and characterization of a PPLN waveguide  
 243 for broadband, mW-level, NIR to MIR wavelength conversion. The generated MIR light was



244 tuned by changing the wavelength of a 1.02 - 1.065  $\mu\text{m}$  pump and a telecom C-band signal.  
245 Compared to conventional TFLN waveguides on silica devices [15], the here-proposed waveguide  
246 configuration benefits from a larger cross-section to achieve better mode confinement and lower  
247 propagation and coupling losses, thus allowing higher optical power levels for the generated idler.  
248 The demonstrated broadband fine-tuning in the  $\approx 3 - 3.5 \mu\text{m}$  wavelength range, achievable output  
249 power level and the capability of translating the mature telecom technology in the MIR can be  
250 exploited for spectroscopy applications. Higher powers and broader conversion bands may be  
251 demonstrated in the future by improving the input laser sources and changing the chip temperature.  
252 Further progress in the realization of the poling mask may also enable the exploitation of the  
253 entire length of the waveguide for the DFG nonlinear process, increasing both efficiency and  
254 achievable output power.

255 **Funding.** This work is part of the project NODES which has received funding from the MUR – M4C2 1.5  
256 of PNRR funded by the European Union - NextGenerationEU (Grant agreement no. ECS00000036) and  
257 has been also funded by the European Project ACTPHAST 4R4R-IPP-20210405. It has also been partially  
258 funded by the NanoFiLN project (ANR-23-PEEL-0004).

259 **Acknowledgments.** We acknowledge the support of the French RENATECH network through its  
260 FEMTO-ST technological facility.

## 261 References

- 262 1. U. Willer, M. Saraji, A. Khorsandi, *et al.*, “Near- and mid-infrared laser monitoring of industrial processes,  
263 environment and security applications,” *Opt. Lasers Eng.* **44**, 699–710 (2006). Optical Diagnostics and Monitoring:  
264 Advanced monitoring techniques and coherent sources.
- 265 2. M. V. Reboucas, J. B. dos Santos, D. Domingos, and A. R. C. Massa, “Near-infrared spectroscopic prediction of  
266 chemical composition of a series of petrochemical process streams for aromatics production,” *Vib. Spectrosc.* **52**,  
267 97–102 (2010).
- 268 3. L. DRS, “MIRcat™ Mid-IR Laser: Tune 1000 cm-1 at 1000s cm-1/s | High-Speed Tuning — daylight solutions.com,”  
269 <https://www.daylightsolutions.com/products/mircat/> (2024). 07/19/2024.
- 270 4. Q. Lu, D. Wu, S. Sengupta, *et al.*, “Room temperature continuous wave, monolithic tunable THz sources based on  
271 highly efficient mid-infrared quantum cascade lasers,” *Sci. Reports* **6**, 23595 (2016).
- 272 5. F. Xie, C. Caneau, H. LeBlanc, *et al.*, “Room Temperature CW Operation of Short Wavelength Quantum Cascade  
273 Lasers Made of Strain Balanced GaIn1-xAs/AlyIn1-yAs Material on InP substrates,” *IEEE J. Sel. Top. Quantum  
274 Electron. - IEEE J SEL TOP QUANTUM ELECTRON* **17**, 1445–1452 (2011).
- 275 6. I. Vurgaftman, R. Weih, M. Kamp, *et al.*, “Interband cascade lasers,” *J. Phys. D: Appl. Phys.* **48**, 123001 (2015).
- 276 7. W. W. Bewley, C. L. Canedy, C. S. Kim, *et al.*, “High-power room-temperature continuous-wave mid-infrared  
277 interband cascade lasers,” *Opt. Express* **20**, 20894–20901 (2012).
- 278 8. W. Geng, Y. Fang, Y. Wang, *et al.*, “Nonlinear photonics on integrated platforms,” *Nanophotonics* **13**, 3253–3278  
279 (2024).
- 280 9. V. Vitali, I. Demirtzioglou, C. Lacava, and P. Petropoulos, “Nonlinear signal processing on chip,” in *On-Chip  
281 Photonics*, (Elsevier, 2024), pp. 273–296.
- 282 10. D. Zhu, L. Shao, M. Yu, *et al.*, “Integrated photonics on thin-film lithium niobate,” *Adv. Opt. Photonics* **13**, 242–352  
283 (2021).
- 284 11. B. You, S. Yuan, Y. Tian, *et al.*, “Lithium niobate on insulator – fundamental opto-electronic properties and photonic  
285 device prospects,” *Nanophotonics* (2024).
- 286 12. Y. Qi and Y. Li, “Integrated lithium niobate photonics,” *Nanophotonics* **9**, 1287–1320 (2020).
- 287 13. M. Xu, M. He, H. Zhang, *et al.*, “High-performance coherent optical modulators based on thin-film lithium niobate  
288 platform,” *Nat. Commun.* **11**, 3911 (2020).
- 289 14. D. Pohl, M. Reig Escalé, M. Madi, *et al.*, “An integrated broadband spectrometer on thin-film lithium niobate,” *Nat.  
290 Photonics* **14**, 24–29 (2020).
- 291 15. J. Mishra, T. P. McKenna, E. Ng, *et al.*, “Mid-infrared nonlinear optics in thin-film lithium niobate on sapphire,” in  
292 *2021 Conference on Lasers and Electro-Optics (CLEO)*, (2021), pp. 1–2.
- 293 16. S. Liang, Y. Jung, K. R. H. Bottrill, *et al.*, “L-band Mode and Wavelength Conversion in a Periodically Poled Lithium  
294 Niobate Ridge Waveguide,” in *European Conference on Optical Communication (ECOC) 2022*, (Optica Publishing  
295 Group, 2022), p. Tu5.22.
- 296 17. J. Mishra, M. Jankowski, A. Y. Hwang, *et al.*, “Ultra-broadband mid-infrared generation in dispersion-engineered  
297 thin-film lithium niobate,” *Opt. Express* **30**, 32752–32760 (2022).
- 298 18. C. Hu, A. Pan, T. Li, *et al.*, “High-efficient coupler for thin-film lithium niobate waveguide devices,” *Opt. Express* **29**,  
299 5397–5406 (2021).



- 300 19. L. Deng, X. Gao, Z. Cao, *et al.*, “Improvement to Sellmeier equation for periodically poled LiNbO<sub>3</sub> crystal using  
301 mid-infrared difference-frequency generation,” *Opt. Commun.* **268**, 110–114 (2006).
- 302 20. E. Courjon, N. Courjal, W. Daniau, *et al.*, “Lamb wave transducers built on periodically poled Z-cut LiNbO<sub>3</sub> wafers,”  
303 *J. Appl. Phys.* **102**, 114107 (2007).
- 304 21. R. Kou, S. Kurimura, K. Kikuchi, *et al.*, “High-gain, wide-dynamic-range parametric interaction in Mg-doped  
305 LiNbO<sub>3</sub> quasi-phase-matched adhered ridge waveguide,” *Opt. Express* **19**, 11867–11872 (2011).
- 306 22. S. Kurimura, Y. Kato, M. Maruyama, *et al.*, “Quasi-phase-matched adhered ridge waveguide in LiNbO<sub>3</sub>,” *Appl.*  
307 *Phys. Lett.* **89**, 191123–191123 (2006).
- 308 23. M. Chauvet, F. Henrot, F. Bassignot, *et al.*, “High efficiency frequency doubling in fully diced LiNbO<sub>3</sub> ridge  
309 waveguides on silicon,” *J. Opt.* **18**, 085503 (2016).
- 310 24. M. F. Volk, S. Suntsov, C. E. Rüter, and D. Kip, “Low loss ridge waveguides in lithium niobate thin films by optical  
311 grade diamond blade dicing,” *Opt. Express* **24**, 1386–1391 (2016).
- 312 25. N. Courjal, B. Guichardaz, G. Ulliac, *et al.*, “High aspect ratio lithium niobate ridge waveguides fabricated by optical  
313 grade dicing,” *J. Phys. D: Appl. Phys.* **44**, 305101 (2011).
- 314 26. D. Hofstetter and R. L. Thornton, “Theory of loss measurements of Fabry–Perot resonators by Fourier analysis of the  
315 transmission spectra,” *Opt. Lett.* **22**, 1831–1833 (1997).
- 316 27. M. Vainio and L. Halonen, “Mid-infrared optical parametric oscillators and frequency combs for molecular  
317 spectroscopy,” *Phys. Chem. Chem. Phys.* **18**, 4266–4294 (2016).
- 318 28. V. Pecheur, H. Porte, J. Hauden, *et al.*, “Watt-level SHG in undoped high step-index PPLN ridge waveguides,” *OSA*  
319 *Continuum* **4**, 1404–1414 (2021).